PHOTONICS Research

Birefringent transmissive metalens with an ultradeep depth of focus and high resolution

JIARAN QI,* YONGHENG MU, SHAOZHI WANG, ZHIYING YIN, AND JINGHUI QIU

Department of Microwave Engineering, Harbin Institute of Technology, Harbin 150001, China
**Corresponding author: qi.jiaran@hit.edu.cn*

Received 4 November 2020; revised 30 December 2020; accepted 2 January 2021; posted 5 January 2021 (Doc. ID 414181); published 11 February 2021

Depth of focus (DOF) and transverse resolution define the longitudinal range and definition of the focusing lens. Although metasurface axilenses and light-sword metalenses with radial and angular modulations can elongate the DOF, these approaches have inherent limitations in being reliable only for small numerical aperture (NA) cases, which in turn compromises the transverse resolution for the given aperture dimension. To conquer this limitation, we propose and experimentally demonstrate a birefringent metalens, achieving an ultradeep DOF of 41λ in terms of the total scattered field, corresponding to a record-breaking wide NA range from 0.14 to 0.7. Meanwhile, the diffraction limited focal spot size in this NA range can guarantee acquisition of images with high resolution. A hybrid methodology is proposed that utilizes both the accuracy of holography in electromagnetic field reconstruction and the polarization multiplexing to double the DOF. A stratified transmissive meta-atom is utilized to encode a pair of independent phase profiles in two orthogonal polarization channels. Furthermore, we combine the generalized scattering matrix with the multipole expansion theory for the first time to elucidate the mechanism of maintaining high transmittance and widening the transmission phase coverage by using the multilayered structure. The proposed metalens provides a competitive platform for devising high-resolution deep DOF systems for imaging and detection applications.

https://doi.org/10.1364/PRJ.414181

1. INTRODUCTION

Depth of focus (DOF) and transverse resolution, which determine longitudinal range and the definition of a focusing lens, are two important technical parameters of imaging systems [1–3]. Deep DOF lenses have received continuously growing interest due to the increasing practical demands for high resolution focusing capabilities in an extended lateral range. However, traditional solutions, such as light-sword optical elements, forward logarithmic axicons, and inverse quartic axicons, achieve desired phase profiles by propagation phase accumulation in the dielectric materials [4–6]. The continuous phase contour places critical demand on the surface curvature of lenses, resulting in tremendous fabrication challenges [7–9]. Also, bulky and nonplanar shapes may increase the difficulty in system integration, which limits their further practical applications [10–13]. Alternatively, metasurfaces and the two-dimensional modality of metamaterials, have produced considerable advances in compact spatial-light-modulation devices, such as functionality multiplexing, owing to their flexible regulation of electromagnetic wavefronts and lower complexity in fabrication [14–20]. With the capability of engineering amplitude, phase, and polarization of electromagnetic waves over subwavelength thickness [21–30], metalenses exhibit significant superiorities over traditional lenses. Novel deep DOF metalenses are mainly developed by ring segmentation of the aperture, radial modulation (RM), and angular modulation (AM) [31,32]. The ring segmentation method divides the metalens aperture into multiple concentric rings so that the illuminating beam impinging on each ring region is focused at a different focal position. It is often used to implement nondiffractive beams such as Bessel beams [33–37]. However, segmentation leads to low aperture utilization efficiency, resulting in relatively large aperture size and thus limiting practical applications of the metalenses. The RM and AM obtain phase profiles of the metalens analytically based on quasi-optical technology and ideally require a continuous phase variation profile on the metalens. Nevertheless, only under the condition of a small numerical aperture (NA), can the discrete pixels on the metalens be approximately treated as the ideal point source, and the phase profile is thus roughly continuous. Otherwise, these aforementioned design methodologies will generate large error in terms of the generated focal length and DOF. Therefore, these methods are suitable for deep DOF metalens design in a small NA scenario. An entirely different route for the DOF extension is to adopt the meta-atom supporting polarization multiplexing, e.g., Y-shaped nanoantennas and interleaved nanorods [26]. These metalenses

enable simultaneous focusing of two orthogonally polarized beams, which thereby doubles the DOF achieved in a single polarization case [38–40]. However, the Y-shaped nanoantenna operates in the reflection mode and is thus not a favorable solution for practical metalens implementation. Moreover, their asymmetric structure may result in focal spot deformation when the constituent metalens is offset-illuminated. As for the meta-atom composed of interleaved nanorods, which regulate the illuminating beams of different polarizations, nonnegligible cross talk may be encountered and complicate the design process. The desired phase profiles of the corresponding metalens are usually obtained by the RM only suitable for a small NA scenario or the time-consuming genetic algorithm, making it impossible to achieve the deepest possible DOF. Indeed, metalenses of small NAs can construct more uniform focal spot sizes within the entire DOF. However, this inevitably leads to an imaging system of relatively low resolution.

Here, we demonstrate an ultracompact high transverse-resolution metalens with ultradeep DOF in the microwave region. The metalens is composed of the birefringent cross I-shaped meta-atoms, enabling flexible and independent phase regulation of two orthogonal linearly polarized electromagnetic waves. Unlike Y-shaped nanoantennas and interleaved nanorods, the meta-atom operates in the transmission mode and can realize independent modulation on two orthogonal polarization modes. In addition, we apply a modified weighted Gerchberg–Saxton method (GSWm) to retrieve phase profiles of the metalens, conquering the precision issue encountered by RM and AM for a large NA scenario [41–45]. Benefiting from the high efficiency and flexibility of GSWm, the metalens can perform large NA high-resolution focusing, and meanwhile realize the deepest possible DOF for each single polarization state. The proof-of-concept metalens experimentally enables a DOF of near 41λ in a record-breaking wide NA range from 0.14 to 0.7. In addition, we combine the generalized scattering matrix with the multipole expansion theory for the first time to elucidate the physical mechanism of the stratified meta-atom.

2. DESIGN AND METHOD

A. Principle of Metalens and Birefringent Meta-Atom Design

The schematic diagram of the proposed ultradeep DOF metalens with a high transverse resolution is illustrated in Fig. 1. Considering the positive correlation between resolution and NA, lenses designed based on RM or AM actually sacrifice focal spot size to achieve a long DOF. Owing to the accuracy of holography in electromagnetic field reconstruction, the proposed metalens decouples the inherent correlation between the DOF and NA in RM and AM. Furthermore, this birefringent metalens can be interpreted as a polarization multiplexing metalens for x- and y-linearly polarized electromagnetic waves. These two beams, orthogonally decomposed components of a normally incident linearly polarized beam with a polarization angle $\theta = 45°$, are modulated by the metalens to generate two focused beams. The subsequent polarization combination roughly doubles the maximum DOF achieved with single polarization.

To suppress the cross talk between different polarization channels and thus facilitate the design process, we utilize the stratified cross I-shaped meta-atom that can independently manipulate the phase of x- and y-polarized electromagnetic waves while maintaining the same transmittance, as detailed in Fig. 2(a). Three layers of dielectric substrates with etched metal square lattices are aligned at a separation of $h = 9.2$ mm, where the relative permittivity of the dielectric substrate is 2.85 with a loss tangent of 0.001, and the cross I-shaped slot is located at the center of the square metal lattice. The thickness of the metal lattice and dielectric substrate is $h_m = 0.035$ mm and $h_s = 1.016$ mm. The side length of the meta-atom is $P = 10$ mm, while d, l_x, l_y, and l_s are the geometrical parameters of the slot. The central cross slot remains unchanged and is applied to connect two pairs of orthogonal marginal slots so that the element structure has a proper electrical length to interact more efficiently with the impinging electromagnetic wave. Figure 2(b)

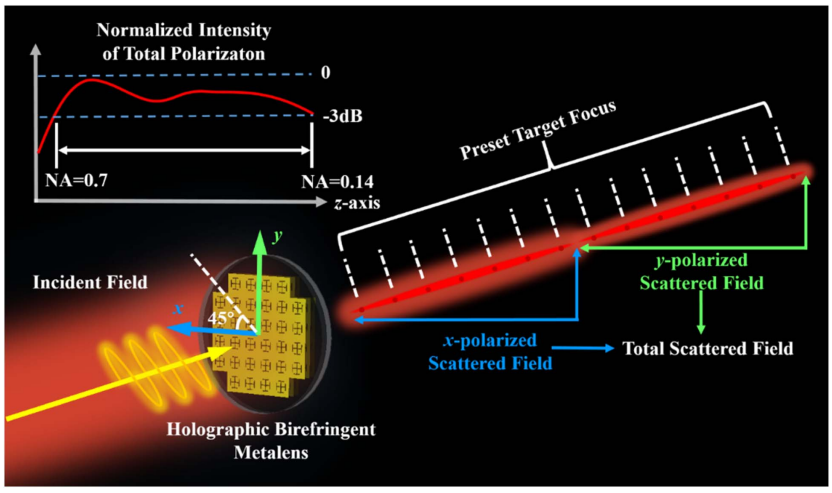

Fig. 1. Schematic diagram of proposed birefringent metalens with ultradeep DOF. The incident linearly polarized electromagnetic wave can be decomposed into two orthogonal parts, i.e., the x-polarized (E_x) and y-polarized (E_y) beams. The birefringent metalens is able to modulate E_x or E_y independently. Holography can be applied to set several foci along the z axis (the optical axis of the metalens) for E_x and E_y beams to realize ultradeep DOF.

shows the surface current distributions on the meta-atom when excited by the x- and the y-polarized electromagnetic waves, respectively. The surface current is mainly distributed on the four marginal bars so that the length variation of the marginal slots can achieve the required transmission phase changes. Furthermore, the independent responses of the horizontal and the vertical slots to the x- and the y-polarized illuminations indicate the birefringent characteristics of the meta-atom. Such a high polarization isolation level, greatly simplifying the meta-atom library construction, can also be witnessed in Fig. 2(c), where the variation of the horizontal length l_x has little influence on the amplitude and phase profiles of the transmitted y-polarized wave, and vice versa. It is also shown that the meta-atom has an over 300° phase coverage, with a transmission amplitude greater than 0.7. The low transmittance and the distorted phase variation in the lower right corner of Fig. 2(c) are caused by the near intersection of two slots, resulting from excessive values of l_x and l_y. As shown in Fig. 2(a), three identical cross I-shaped meta-atoms are stacked, which improves the transmittance as well as the transmission phase coverage when varying geometrical details of the meta-atom. Compared to stacked structures with layers of different geometrical details, this configuration will not introduce extra parameters to be further optimized, greatly simplifying the process of the meta-atom library construction. It is also noted that the existing mechanism analysis of such a stratified meta-atom is based on the scattering matrix cascade. For instance, the relation between the transmission phase limit and the layer number was predicted by this approach [46]. Here, we first apply the generalized scattering matrix [47] to demonstrate the coherent relation between high transmission amplitude and entire phase coverage of an arbitrary multi-layered meta-atom. The multipole expansion theory [48–50] is then applied to specify the underlying principle of maintaining high transmission amplitude while varying the geometrical details of the utilized meta-atom.

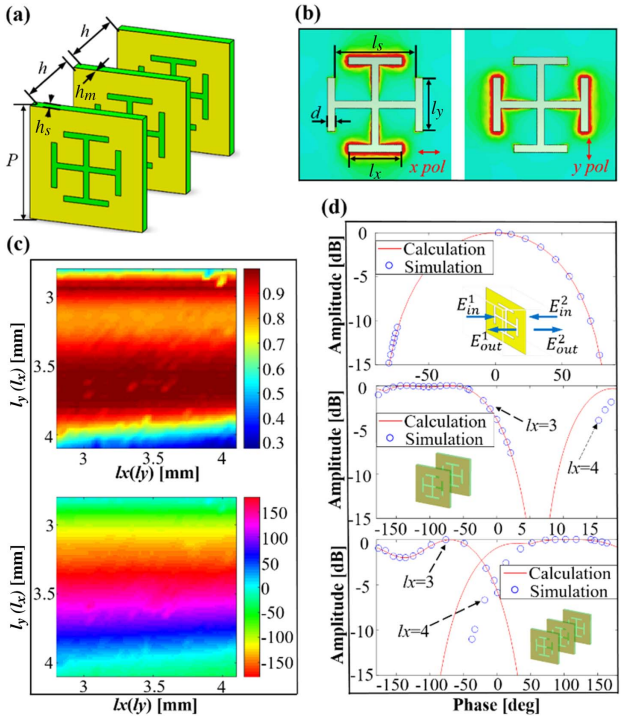

Fig. 2. Building blocks, and calculation and simulation results of relation between transmission amplitude and phase. (a) Schematic diagram of the triple-layered cross I-shaped meta-atom; (b) surface current distribution under the illumination of the x- and the y-polarized beams, respectively; (c) simulated transmission amplitude and phase by sweeping l_x and l_y at 10 GHz; (d) transmission phase coverage of single-, double-, and triple-layered cross I-shaped meta-atoms against the transmission amplitude. The insets are the schematic diagrams of the two-port networks calculated by the scattering matrix.

First of all, we decompose an arbitrary single-layered metal–dielectric square meta-atom into a metal sheet and a dielectric substrate, whose scattering matrices can be separately modeled, as shown in detail in Appendix A.1. Thus, for a stratified structure, its generalized scattering matrix can be formulated by successively cascading the scattering matrices of every single-layered meta-atom and interlayer air gap. For the dielectric substrate, the scattering parameters can be written as

$$S_{11} = S_{22} = \frac{\Gamma(1 - e^{-j2\beta L_d})}{1 - \Gamma^2 e^{-j2\beta L_d}},$$
$$S_{12} = S_{21} = \frac{(1 - \Gamma^2)e^{-j\beta L_d}}{1 - \Gamma^2 e^{-j2\beta L_d}}, \quad (1)$$

where Γ, β, and L_d correspond to reflection coefficient, phase-shift constant, and thickness of the dielectric substrate. With the symmetric ($S_{11} = S_{22}$), reciprocal ($S_{12} = S_{21}$), and lossless ($\sum_{j=1}^{2} |S_{ji}|^2 = 1$, $i = 1, 2$ and $S_{11}S_{12}^* + S_{21}S_{22}^* = 0$) assumptions, one can finally express all scattering parameters of the square metal lattice as functions of the transmission phase, which read

$$S_{11} = \sin(\angle S_{21})e^{j(\angle S_{21} \pm \frac{\pi}{2})}, \qquad S_{21} = \cos(\angle S_{21})e^{j(\angle S_{21})}. \quad (2)$$

Therefore, we can analytically study the monochromatic coherent relation between transmission amplitude and phase. The red solid line in Fig. 2(d) illustrates the theoretically predicted transmission amplitude variation with the phase for single-, double-, and triple-layered meta-atoms composed of the arbitrary metal–dielectric square lattice, similar to that shown in Fig. 2(a). The simulation results are provided as validations. It should be noted that every small blue circle represents the simulated transmission amplitude and phase of a certain cross I-shaped meta-atom with l_x of a fixed value. In general, good agreement can be observed, although for double- and triple-layered meta-atoms, while l_x or l_y is relatively large, the simulation results slightly deviate from theoretical analysis due to the cross talk of orthogonally polarized beams, resulting from the close distance of slots. For a single-layered meta-atom, the phase covers about 100°, with the transmission amplitude larger than −2 dB. By adding extra layers, the phase coverage gradually grows, and a triple-layered meta-atom can extend the phase coverage to a complete 360°. This monochromatic analysis thus confirms that, in theory, a stratified meta-atom can effectively broaden the phase coverage while maintaining a high transmittance level. It further implies that if one can maintain

the transmission amplitude while varying the geometrical details of the meta-atom, the phase coverage can be effectively extended.

The extinction spectra of a scatterer with near-zero absorption can indirectly measure its transmittance due to the absence of absorbance [48–50]. They are determined by the multipole moments that the electromagnetic illumination can excite in the scatterers, which reads

$$\sigma_{\text{ext}} = -\frac{\pi}{k^2}\sum_{l=1}^{\infty}\sum_{m=-1,\,1}(2l+1)\text{Re}[m a_E(l,m) + a_M(l,m)], \tag{3}$$

where the integer l represents the order of the multipole, and the integer m ranges from $-l$ to l.

The relevant multipole contributions $a_E(l,m)$ and $a_M(l,m)$ can further be calculated by the electromagnetic multipole expansion, as shown in detail in Appendix A.2. The method is successively applied to analyze extinction spectra of single-, double-, and triple-layered cross I-shaped meta-atoms with $l_x = l_y = 3.5$ mm at the vicinity of the wavelength 30 mm. Figure 3(a) illustrates the extinction spectrum decomposition by multipole expansion of the single-layered meta-atom in the air excited by a normally incident x-polarized wave. It is shown that the electric dipole plays a dominant role in this scenario. However, by stacking up multiple layers, the dominant modes expand to magnetic dipole and high-order multipoles, including electric quadrupole and magnetic quadrupole, as shown in Figs. 3(b) and 3(c). The superposition of multipole effects results in a larger extinction coefficient, as shown in Fig. 3(d), which implies that the multilayered meta-atom can maintain a high transmittance in a wide frequency range. Furthermore, Fig. 3(e) illustrates the monochromatic relation between the extinction coefficients and geometrical details. It is indicated that due to contributions of the magnetic dipole and high-order multipoles, the triple-layered meta-atom can maintain a large extinction coefficient with varying geometrical details. In particular, the shadowed area in Fig. 3(e) indicates the geometrical range of l_x (l_y) of the selected meta-atoms composing the metalens, which corresponds to that illustrated in Fig. 2(c) and ranges from 2.9 to 3.85 mm when the transmission amplitude is greater than 0.7. Therefore, it is elucidated by multipole expansion theory that the multilayered cross I-shaped meta-atom can support rich higher-order modes to maintain its high transmittance with varying geometrical details. Furthermore, by the generalized scattering matrix, a broad transmission phase coverage can be simultaneously guaranteed.

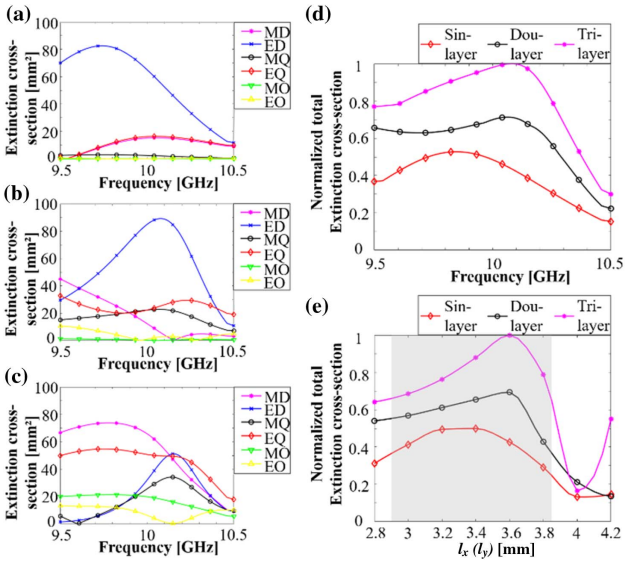

Fig. 3. Extinction cross-sectional spectra of the cross I-shaped meta-atoms in air for the x-polarized normal incidence. Extinction cross-sectional spectra of (a) single-, (b) double-, and (c) triple-layered cross I-shaped meta-atoms. MD represents magnetic dipole, ED represents electric dipole, MQ represents magnetic quadrupole, EQ represents electric quadrupole, MO represents magnetic octupole, and EO represents electric octupole. (d) Normalized total extinction cross-sectional spectra of single-, double-, and triple-layered cross I-shaped meta-atoms under the condition of $l_x = l_y = 3.5$ mm; (e) monochromatic variation of normalized total extinction cross section with l_x (l_y) at 10 GHz.

B. Birefringent Metalens Based on the Modified GSW Method

The utilized meta-atom provides a powerful physical platform for the realization of a polarization multiplexing metalens with an ultradeep DOF. We will further show how to determine accurately the phase profiles of the metalens in a large NA scenario. As aforementioned, we adopted the GSWm to obtain the desired phase profiles. We discretize the preset fields as a series of field concentration points with customized intensities along the optical axis, as shown in Fig. 1. Corresponding phase profiles of the metalens can then be defined as

$$\phi_n = \arg\left(\sum_{m=1}^{M}\frac{e^{jkr_{mn}}}{r_{mn}}\frac{w_m V_m}{|V_m|}\right), \tag{4}$$

where r_{mn} denotes the distance between the nth out of N pixels in metalens and the mth out of M target points, and V_m denotes the vector superposition of the scattering field emitted from each pixel of the metalens to the mth target point of preset fields. The weighting factor w_m is applied to adjust the reconstruction accuracy of different preset field points. To improve the robustness of GSW, the relaxation factor p is introduced to scale dynamically w_m for the ith step in an iteration procedure, which reads

$$w_m^i = w_m^{i-1}\left(\frac{\langle|V_m^{i-1}|\rangle}{|V_m^{i-1}|}\right)^p, \tag{5}$$

$$\phi_n^i = \arg\left(\sum_{m=1}^{M}\frac{e^{jkr_{mn}}}{r_{mn}}\frac{w_m^i V_m^{i-1}}{|V_m^{i-1}|}\right). \tag{6}$$

It is worth mentioning that GSWm reduces to GS and GSW when p is equal to 0 and 1, respectively. To investigate the influence of the index p on the robustness of GSWm, we calculate the sum-squared error (SSE) when p takes different values. The SSE is defined by

$$\mathrm{SSE} = \frac{\sum (|V_m| - \langle V_m \rangle)^2}{\sum |V_m|^2}. \tag{7}$$

3. NUMERICAL AND EXPERIMENTAL RESULTS

Figure 4(a) shows the SSE curve against the iteration step for different p. The preset field concentration points are positioned along the z axis from 180 to 600 mm with a fixed separation distance of 30 mm. To eliminate the influence of the initial phase profile on the metalens, all initial ϕ_n^0 are set to 0. It is apparent that a robust convergence can be achieved when $p = 0.5$. Otherwise, SSE fluctuations will possibly be encountered, e.g., $p = 1$ or 1.2. Thus, by properly adjusting the value of p and intervals between adjacent field concentration points, the phase profiles for the x and y polarizations on the metalens can be retrieved, as shown in Fig. 4(b). The convergence criterion is to maximize the DOF, within which a less than 3 dB energy variation along the optical axis should be satisfied. For x polarization, the distance between the metalens and every field concentration point ranges from 7λ to 23λ, with a 2λ interval between adjacent points. Similarly, for y polarization, the distance ranges from 25λ to 46λ, with a 3λ interval. Such a configuration, abiding by essentially the physical properties of the field distribution around the focal spot of a lens, leads to good convergences, as shown in Fig. 4(c). The field distribution in the xoz plane is theoretically calculated by the Fresnel diffraction theory, assuming that the amplitude distribution on the metalens is uniform and the phase profiles follow those in Fig. 4(b). The field-intensity distributions of x-polarized, y-polarized, and total scattered fields are shown in Figs. 4(d)–4(f). The field distribution in the xoz plane is identical to that in the yoz plane due to the rotational symmetry of the phase and amplitude profiles. The calculated field distribution along the z axis is shown in Fig. 4(g), where the DOFs of the x-polarized (E_x) and the y-polarized (E_y) scattered fields are 452 mm from $z = 208$ mm to 660 mm, and 933 mm from $z = 667$ mm to 1600 mm. The DOF according to the total scattered field ($E_{\mathrm{total}} = \sqrt{E_x^2 + E_y^2}$) obtained after polarization recombination reads 1271 mm from $z = 199$ mm to 1470 mm, and the corresponding NA ranges from 0.14 to 0.73.

Finally, a proof-of-concept birefringent metalens prototype in the microwave region is implemented and fabricated for experiments. A normally incident beam with a linear polarization angle $\theta = 45°$ and a wavelength of 30 mm illuminates the metalens composed of 42×42 cross I-shaped meta-atoms. The full-wave simulation results of E_x, E_y, and E_{total} in the xoz plane at 10 GHz are shown in Figs. 4(h)–4(j). The normalized field-intensity distributions along the z axis are shown in Fig. 4(k), and the DOFs according to E_x, E_y, and E_{total} are 260 mm from $z = 190$ mm to 450 mm, 979 mm from $z = 517$ mm to 1496 mm, and 1290 mm from $z = 185$ mm to 1475 mm. The corresponding NA ranges from 0.14 to 0.75, which agrees well with the theoretical predictions. The experiment results of E_x, E_y, and E_{total} along the z axis are presented in Fig. 5(a). The DOF of the metalens is 1230 mm (41λ) from $z = 220$ mm (7.3λ) to 1450 mm (48.3λ), and the corresponding NA range is from 0.14 to 0.7. Furthermore, Fig. 5(b) illustrates the field-intensity comparison along the optical axis by calculation, simulation, and experiment. The deviation of the experiment results from the others, especially in the large NA case, mainly results from the spherical wavefronts radiated by the applied

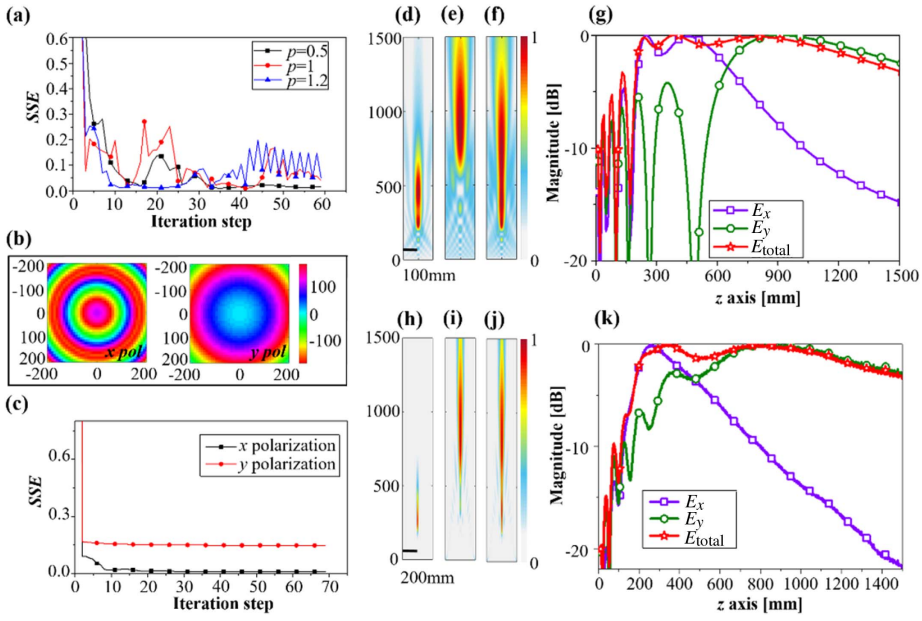

Fig. 4. GSWm and the design process of the birefringent metalens. (a) Comparison of convergence characteristics under different values of p; (b) phase profiles of the x and the y polarizations by GSWm; (c) SSE curve during the phase profiles calculation process of the x and y polarizations in the metalens; normalized intensity in the xoz plane of (d) E_x, (e) E_y, and (f) E_{total} calculated by Fresnel diffraction theory. The normalized intensity along the z axis is shown in (g). The full-wave simulation results of the normalized intensity in the xoz plane of (h) E_x, (i) E_y, and (j) E_{total}; (k) normalized intensity along the z axis.

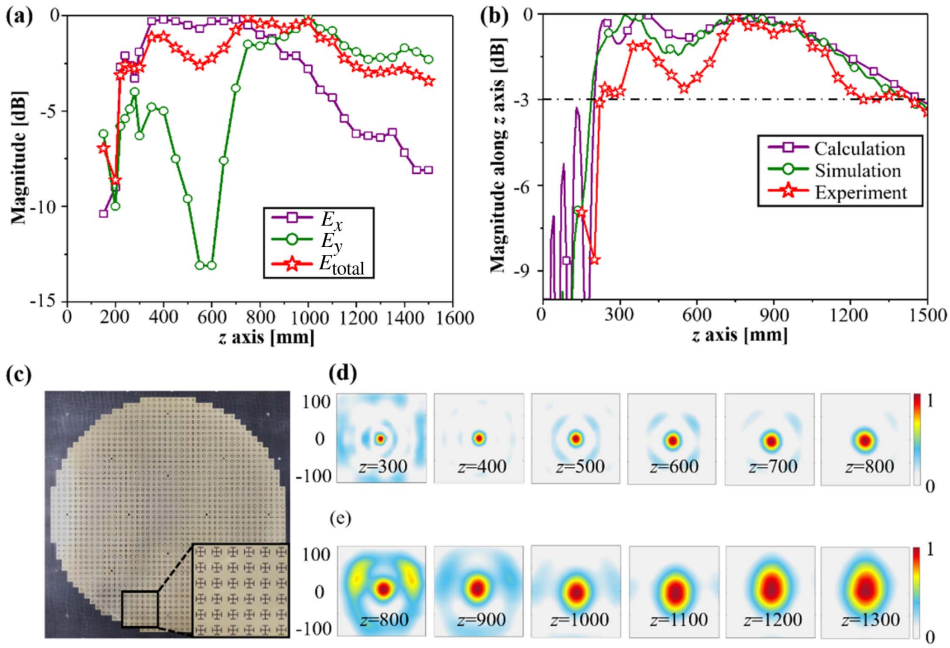

Fig. 5. Fabricated metalens and experiment results. (a) Experiment results of normalized intensities along the z axis for E_x, E_y, and E_{total}; (b) normalized intensities of the total scattered field by calculation, simulation, and experiment; (c) fabricated sample of the designed metalens by GSWm; inset is a zoomed-in view of the prototype; normalized field-intensity distribution for (d) E_x, (e) E_y at different longitudinal distances.

standard horn antenna and influence of the diffracted wave. Figure 5(c) illustrates the fabricated metalens prototype; the inset shows its detailed configuration. The normalized field-intensity distributions of E_x and E_y at different cutting planes transverse to the optical axis are shown in Figs. 5(d) and 5(e). As the distance between the metalens and the focal plane increases, the focal spot size also becomes larger, but still close to the corresponding diffraction limit. It is noted that the focal spot becomes elliptic for a larger focal length, e.g., $z = 1200$ mm or 1300 mm. This phenomenon may result from the asymmetric radiation pattern of the feed horn antenna and misalignment between the feed's main beam and the metalens' optical axis, which have more obvious influences on the focal spot shape for a larger focal length.

To further validate the ultradeep DOF imaging capability of the metalens, full-wave simulation results of high transverse-resolution imaging in the longitudinal direction are shown. To achieve the imaging function, an extra focal point needs to be implemented on the other side of the metalens, and we fix the focal length as 120 mm. Therefore, the phase profiles for the x and y polarizations on the metalens can be defined as

$$\phi'_{x,y} = \phi_{x,y} + 2\pi\left[\sqrt{f_0^2 + (x^2 + y^2)} - f_0\right]\Big/\lambda, \qquad (8)$$

where $\phi_{x,y}$ denotes the phase profiles by the GSWm for the x and the y polarizations shown in Fig. 4(b), and the latter part of Eq. (8) denotes those compensating the accumulated propagation phase difference from this fixed focal point to different locations on the metalens. The full-wave simulated field distribution for E_{total} under the illumination of the linearly polarized spherical wave with a polarization angle of 45° at 10 GHz is illustrated in Fig. 6(a). The DOF of the metalens is 1204 mm (40.1λ) from $z = 280$ mm (9.3λ) to 1484 mm (49.5λ), and the corresponding NA range is from 0.14 to 0.6. The converging effect based on the quasi-optical technology generates a large error in terms of the generated focal length under the condition of a large NA, which further illustrates the advantages of GSWm to calculate the phase profiles. A square

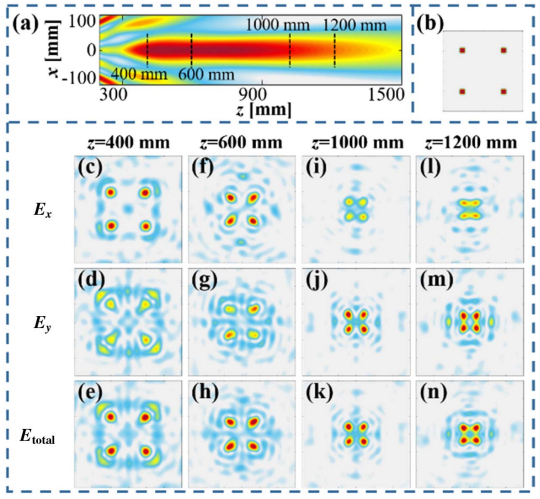

Fig. 6. High transverse-resolution imaging simulation results. (a) Full-wave simulated results of normalized intensities along the z axis for E_{total} under the illumination of linearly polarized spherical wave with a polarization angle of 45° at 10 GHz; (b) square pattern consisting of four discrete points; simulated field distributions for E_x, E_y, and E_{total} when the square pattern is placed at (c)–(e) $z = 400$ mm, (f)–(h) $z = 600$ mm, (i)–(k) $z = 1000$ mm, and (l)–(n) $z = 1200$ mm.

pattern consisting of four discrete points [see Fig. 6(b)] is designed for imaging at different distances from the metalens, represented by the black dotted lines in Fig. 6(a). It should be noted that in this numerical validation, the distance between the metalens and the imaging plane is fixed. Figures 6(c)–6(h) show the simulated field distributions for E_x, E_y, and E_{total} when the square pattern is placed at $z = 400$ mm and $z = 600$ mm. The scaled pattern is observed in the field distribution of E_x. The total scattered field is mainly composed of E_x components. However, for $z = 1000$ mm and $z = 1200$ mm, the scaled pattern can be more obviously observed in the field distribution of E_y, and the total scattered field is mainly composed of the E_y component, as shown in Figs. 6(i)–6(n). The peak signal-to-noise ratio (PSNR), defined as the ratio between peak intensity in the pattern to the standard deviation of the background noise, is adopted here to evaluate the imaging quality. The PSNRs of the simulated results for $z = 400$ mm, $z = 600$ mm, $z = 1000$ mm, and $z = 1200$ mm are found to be 13, 13.8, 15.7, and 15.7, which further validate the metalens high transverse-resolution imaging functionality with an ultradeep DOF.

4. CONCLUSION

In summary, we have theoretically and experimentally proposed a high transverse-resolution transmissive metalens with an ultradeep DOF based on the birefringent stratified cross I-shaped meta-atom and the robust GSWm method. An ultradeep DOF of 1230 mm (41λ) ranging from 220 mm (7.3λ) to 1450 mm (48.3λ), corresponding to a wide NA range from 0.14 to 0.7, is presented under the illumination of a normally incident beam with a linear polarization angle of 45° at the wavelength of 30 mm. More importantly, the focal spot size is close to the corresponding diffraction limit in a wide NA range, which provides high-resolution characteristics for application, overcoming the limitation of previous deep DOF lenses that only adopted small NA focusing. The underlying operational mechanism of stratified meta-atoms is elucidated by the generalized scattering matrix and the multipole expansion theory. Further work will focus on extending the capability of the GSWm to finely shape the three-dimensional near-field distribution. The marriage of such an advanced iterative method with the birefringent stratified meta-atom in this paper will make possible a metalens with an ultra-deep DOF and more uniform focal spot size within it. Due to the size restriction in available microwave anechoic chambers, practical imaging experiments are numerically performed, which further validates our proposed methodology.

APPENDIX A

1. Analysis of the Inherent Relationship between Transmission Amplitude and Phase

The S matrix relates the incident and scattered electromagnetic wave by [46,47]

$$\begin{bmatrix} E_{\text{out}}^x \\ E_{\text{out}}^y \end{bmatrix} = \begin{bmatrix} S_{11} & S_{12} \\ S_{21} & S_{22} \end{bmatrix} \begin{bmatrix} E_{\text{in}}^x \\ E_{\text{in}}^y \end{bmatrix}. \tag{A1}$$

By assuming that the multilayered element is symmetric ($S_{11} = S_{22}$), reciprocal ($S_{12} = S_{21}$), and lossless ($\sum_{j=1}^{2} |S_{ji}|^2 = 1$, $i = 1, 2$ and $S_{11}S_{12}^* + S_{21}S_{22}^* = 0$), we have thus the relationship between reflection phase and transmission phase fixed by

$$\angle S_{11} - \angle S_{21} = \pm\frac{\pi}{2}. \tag{A2}$$

Under the condition that the higher-order harmonics can be omitted and the Fresnel reflection and transmission coefficient is applied, we get

$$S_{21} = 1 + S_{11}. \tag{A3}$$

Substituting Eq. (A2) into Eq. (A3), as the real and imaginary parts of both sides of the equation are equal, we obtain

$$|S_{11}| = \pm\sin(\angle S_{21}), \tag{A4}$$

$$|S_{21}| = \cos(\angle S_{21}). \tag{A5}$$

Therefore, all scattering parameters of square metal lattices depend only on the transmission phase, which read

$$S_{11} = S_{22} = \sin(\angle S_{21})\mathrm{e}^{j(\angle S_{21} \pm \frac{\pi}{2})}, \tag{A6}$$

$$S_{12} = S_{21} = \cos(\angle S_{21})\mathrm{e}^{j(\angle S_{21})}. \tag{A7}$$

For the dielectric substrate, the S matrix can be written as

$$S_{11} = S_{22} = \frac{\Gamma(1 - \mathrm{e}^{-j2\beta L_d})}{1 - \Gamma^2\mathrm{e}^{-j2\beta L_d}}, \tag{A8}$$

$$S_{12} = S_{21} = \frac{(1 - \Gamma^2)\mathrm{e}^{-j\beta L_d}}{1 - \Gamma^2\mathrm{e}^{-j2\beta L_d}}, \tag{A9}$$

where Γ, β, and L_d correspond to the reflection coefficient, phase-shift constant, and the thickness of the dielectric substrate. When the plane wave is incident into general media, Γ and β can be, respectively, written as

$$\Gamma = \frac{1 - \sqrt{\varepsilon_r}}{1 + \sqrt{\varepsilon_r}}, \tag{A10}$$

$$\beta = \frac{2\pi\sqrt{\varepsilon_r}}{\lambda_0}. \tag{A11}$$

When ε_r is equal to 1 or 2.85, Eqs. (A10) and (A11) represent the electromagnetic waves propagating in the air and the dielectric substrate, respectively. Therefore, the scattering fields of the multilayered element can be theoretically calculated by cascading the S matrices corresponding to the air, square metal lattice, and dielectric substrate in order.

2. Electromagnetic Multipole Expansion Analysis of Single-, Double-, and Triple-Layered Cross I-Shaped Meta-Atoms

The field scattered by the cross I-shaped meta-atoms can be represented by the multipole expansion [48–50]. The E field can be written by

$$\mathbf{E}(r, \theta, \phi) = E_0 \sum_{l=1}^{\infty} \sum_{m=-1}^{l} i^l[\pi(2l + 1)]^{1/2}\mathbf{XH}_{lm}, \tag{A12}$$

$$\mathbf{XH}_{lm} = \frac{1}{k}a_E(l, m)\nabla \times \mathbf{Xh}_{lm} + a_M(l, m)\mathbf{Xh}_{lm}, \tag{A13}$$

$$\mathbf{Xh}_{lm} = h_l^{(1)}(kr)\mathbf{X}_{lm}(\theta, \phi), \tag{A14}$$

where $h_l^{(1)}$ and $\mathbf{X}_{lm}$ are the first-kind spherical Hankel function and the normalized vector spherical harmonics function, respectively. The vector functions $\nabla \times h_l^{(1)}(kr)\mathbf{X}_{lm}(\theta,\phi)$ and $h_l^{(1)}(kr)\mathbf{X}_{lm}(\theta,\phi)$ describe the field created by different electric or magnetic multipoles, where the integer l represents the order of the multipole, and the integer m ranges from $-l$ to l. The multipole coefficients $a_E(l,m)$ and $a_M(l,m)$ reveal the electric and magnetic excitations in cross I-shaped meta-atoms.

For electromagnetic scatterers, $a_E(l,m)$ and $a_M(l,m)$ can be extracted by

$$a_E(l,m) = \frac{(-i)^{l-1}k^2\eta O_{lm}}{E_0[\pi(2l+1)]^{1/2}}\int \mathrm{e}^{-im\varphi}[\mathbf{J}(\mathbf{r})_{\mathbf{E1}} + \mathbf{J}(\mathbf{r})_{\mathbf{E2}}]\mathrm{d}^3r, \tag{A15}$$

$$a_M(l,m) = \frac{(-i)^{l-1}k^2\eta O_{lm}}{E_0[\pi(2l+1)]^{1/2}}\int \mathrm{e}^{-im\varphi}[\mathbf{J}(\mathbf{r})_{\mathbf{M1}} + \mathbf{J}(\mathbf{r})_{\mathbf{M2}}]\mathrm{d}^3r, \tag{A16}$$

$$\mathbf{J}(\mathbf{r})_{\mathbf{E1}} = [\psi_l(kr) + \psi_l''(kr)]P_l^m(\cos\theta)\hat{r}\cdot\mathbf{J}(\mathbf{r}), \tag{A17}$$

$$\mathbf{J}(\mathbf{r})_{\mathbf{E2}} = \frac{\psi_l'(\mathrm{kr})}{kr}[\tau_{lm}(\theta)\hat{\theta}\cdot\mathbf{J}(\mathbf{r}) - i\pi_{lm}(\theta)\hat{\varphi}\cdot\mathbf{J}(\mathbf{r})], \tag{A18}$$

$$\mathbf{J}(\mathbf{r})_{\mathbf{M1}} = j_l(kr)[i\pi_{lm}(\theta)\hat{\theta}\cdot\mathbf{J}(\mathbf{r})], \tag{A19}$$

$$\mathbf{J}(\mathbf{r})_{\mathbf{M2}} = j_l(kr)[\tau_{lm}(\theta)\hat{\varphi}\cdot\mathbf{J}(\mathbf{r})], \tag{A20}$$

$$\mathbf{J}(\mathbf{r}) = -i\omega[\varepsilon(\mathbf{r}) - \varepsilon_b]\mathbf{E}(\mathbf{r}), \tag{A21}$$

$$O_{lm} = \frac{1}{l(l+1)^{1/2}}\left[\frac{2l+1}{4\pi}\frac{(l-m)!}{(l+m)!}\right]^{1/2}, \tag{A22}$$

$$\tau_{lm}(\theta) = \frac{\mathrm{d}}{\mathrm{d}\theta}P_l^m(\cos\theta), \tag{A23}$$

$$\pi_{lm}(\theta) = \frac{m}{\sin\theta}P_l^m(\cos\theta), \tag{A24}$$

where P_l^m and ψ_l describe the associated Legendre polynomials and the Riccati–Bessel function, respectively. The most important step for the electromagnetic multipole expansion is to calculate the multipole coefficients, which measure the specific electric and magnetic responses to the external excitations. The integration should be calculated in a spherical surface containing the stratified meta-atom. Therefore, when l is equal to 1, 2, and 3, the corresponding multipole coefficient of the dipole, quadrupole, and octupole can be obtained.

Since the absorption rate of the cross I-shaped meta-atom is negligible, the extinction cross section and the scattering cross section are approximately equal. Therefore, the extinction cross section reads

$$\sigma_{\mathrm{ext}} = -\frac{\pi}{k^2}\sum_{l=1}^{\infty}\sum_{m=-1,1}(2l+1)\mathrm{Re}[ma_E(l,m) + a_M(l,m)]. \tag{A25}$$

Funding. National Natural Science Foundation of China (61671178, 61301013, 61731007).

Acknowledgment. The paper was written through contributions of J. Qi, Y. Mu, and S. Wang. All authors have given approval to the final version of the paper. J. Qi and J. Qiu conceived the idea for this paper. J. Qi, and Y. Mu together formulated and programed the GSWm, elucidated the underlying operational mechanism of the stratified cross I-shaped meta-atom, fabricated the prototypes, and designed the experiments. Y. Mu and S. Wang conducted the measurements.

Disclosures. The authors declare no conflicts of interest.

REFERENCES

1. F. Qin, K. Huang, J. Wu, J. Teng, C. W. Qiu, and M. Hong, "A supercritical lens optical label-free microscopy: sub-diffraction resolution and ultra-long working distance," Adv. Mater. **29**, 1602721 (2017).
2. F. Qin, K. Huang, J. Wu, J. Jiao, X. Luo, C. Qiu, and M. Hong, "Shaping a subwavelength needle with ultra-long focal length by focusing azimuthally polarized light," Sci. Rep. **5**, 9977 (2015).
3. H. Dehez, A. April, and M. Piché, "Needles of longitudinally polarized light: guidelines for minimum spot size and tunable axial extent," Opt. Express **20**, 14891–14905 (2012).
4. K. Petelczyc, S. Bará, A. C. Lopez, Z. Jaroszewicz, K. Kakarenko, A. Kolodziejczyk, and M. Sypek, "Imaging properties of the light sword optical element used as a contact lens in a presbyopic eye model," Opt. Express **19**, 25602–25616 (2011).
5. K. Kakarenko, I. Ducin, K. Grabowiecki, Z. Jaroszewicz, A. Kolodziejczyk, A. Mira-Agudelo, K. Petelczyc, A. Składowska, and M. Sypek, "Assessment of imaging with extended depth-of-field by means of the light sword lens in terms of visual acuity scale," Biomed. Opt. Express **6**, 1738–1748 (2015).
6. J. Ares, R. Flores, S. Bara, and Z. Jaroszewicz, "Presbyopia compensation with a quartic axicon," Optom. Vis. Sci. **82**, 1071–1078 (2005).
7. Y. J. Bao, Y. Yu, H. F. Xu, C. Guo, J. T. Li, S. Sun, Z. K. Zhou, C. W. Qiu, and X. H. Wang, "Full-colour nanoprint-hologram synchronous metasurface with arbitrary hue-saturation-brightness control," Light: Sci. Appl. **8**, 95 (2019).
8. N. Yu and F. Capasso, "Flat optics with designer metasurfaces," Nat. Mater. **13**, 139–150 (2014).
9. A. V. Kildishev, A. Boltasseva, and V. M. Shalaev, "Planar photonics with metasurfaces," Science **339**, 1232009 (2013).
10. Y. J. Bao, Y. Yu, H. F. Xu, Q. L. Lin, Y. Wang, J. T. Li, Z. K. Zhou, and X. H. Wang, "Coherent pixel design of metasurfaces for multidimensional optical control of multiple printing-image switching and encoding," Adv. Funct. Mater. **28**, 1805306 (2018).
11. C. Pfeiffer and A. Grbic, "Metamaterial Huygens' surfaces: tailoring wave fronts with reflectionless sheets," Phys. Rev. Lett. **110**, 197401 (2013).
12. C. K. Dass, H. Kwon, S. Vangala, E. M. Smith, J. W. Cleary, J. Guo, A. Alu, and J. R. Hendrickson, "Gap-plasmon-enhanced second-harmonic generation in epsilon-near-zero nanolayers," ACS Photon. **7**, 174–179 (2020).
13. H. Gao, Y. Wang, X. Fan, B. Jiao, T. Li, C. Shang, C. Zeng, L. Deng, W. Xiong, J. Xia, and M. Hong, "Dynamic 3D meta-holography in visible range with large frame number and high frame rate," Sci. Adv. **6**, eaba8595 (2020).
14. Y. Liang, K. Koshelev, F. C. Zhang, H. Lin, S. R. Lin, J. Y. Wu, B. H. Jia, and Y. Kivshar, "Bound states in the continuum in anisotropic plasmonic metasurfaces," Nano Lett. **20**, 6351–6356 (2020).
15. Y. X. Wang, Z. K. Wang, X. Feng, M. Zhao, C. Zeng, G. Q. He, Z. Y. Yang, Y. Zheng, and J. S. Xia, "Dielectric metalens-based Hartmann-Shack array for a high-efficiency optical multiparameter detection system," Photon. Res. **8**, 482–489 (2020).
16. L. X. Zhu, X. Liu, B. Sain, M. Y. Wang, C. Schlickriede, Y. T. Tang, J. H. Deng, K. F. Li, J. Yang, M. Holynski, S. Zhang, T. Zentgraf, K. Bongs, Y. H. Lien, and G. X. Li, "A dielectric metasurface optical chip for the generation of cold atoms," Sci. Adv. **6**, eabb6667 (2020).
17. H. X. Xu, L. Zhang, Y. Kim, G. M. Wang, X. K. Zhang, Y. M. Sun, X. H. Ling, H. W. Liu, Z. N. Chen, and C. W. Qiu, "Wavenumber-splitting

metasurfaces achieve multichannel diffusive invisibility," Adv. Opt. Mater. **6**, 1800010 (2018).
18. Z. Y. Yang, Z. K. Wang, Y. X. Wang, X. Feng, M. Zhao, Z. J. Wan, L. Q. Zhu, J. Liu, Y. Huang, J. S. Xia, and M. Wegener, "Generalized Hartmann-Shack array of dielectric metalens sub-arrays for polarimetric beam profiling," Nat. Commun. **9**, 4607 (2018).
19. D. M. Lin, P. Y. Fan, E. Hasman, and M. L. Brongersma, "Dielectric gradient metasurface optical elements," Science **345**, 298–302 (2014).
20. Y. Y. Cheng, Y. X. Wang, Y. Y. Niu, and Z. R. Zhao, "Concealed object enhancement using multi-polarization information for passive millimeter and terahertz wave security screening," Opt. Express **28**, 6350–6366 (2020).
21. X. Zang, H. Ding, Y. Intaravanne, L. Chen, Y. Peng, J. Xie, Q. Ke, A. V. Balakin, A. P. Shkurinov, X. Chen, Y. Zhu, and S. Zhuang, "A multi-foci metalens with polarization-rotated focal points," Laser Photon. Rev. **13**, 1900182 (2019).
22. T. Chantakit, C. Schlickriede, B. Sain, F. Meyer, T. Weiss, N. Chattham, and T. Zentgraf, "All-dielectric silicon metalens for two-dimensional particle manipulation in optical tweezers," Photon. Res. **8**, 1435–1440 (2020).
23. B. Yao, X. Zang, Z. Li, L. Chen, J. Xie, Y. Zhu, and S. Zhuang, "Dual-layered metasurfaces for asymmetric focusing," Photon. Res. **8**, 830–843 (2020).
24. X. Zang, Y. Zhu, C. Mao, W. Xu, H. Ding, J. Xie, Q. Cheng, L. Chen, Y. Peng, Q. Hu, M. Gu, and S. Zhuang, "Manipulating terahertz plasmonic vortex based on geometric and dynamic phase," Adv. Opt. Mater. **7**, 1801328 (2019).
25. X. F. Zang, F. L. Dong, F. Y. Yue, C. M. Zhang, L. H. Xu, Z. W. Song, M. Chen, P. Y. Chen, G. S. Buller, Y. M. Zhu, S. L. Zhuang, W. G. Chu, S. Zhang, and X. Z. Chen, "Polarization encoded color image embedded in a dielectric metasurface," Adv. Mater. **30**, 1707499 (2018).
26. M. Veysi, C. Guclu, O. Boyraz, and F. Capolino, "Reflective metasurface lens with an elongated needle-shaped focus," J. Opt. Soc. Am. B **34**, 374–382 (2017).
27. X. Y. Li, S. B. Wei, G. Y. Cao, H. Lin, Y. J. Zhao, and B. H. Jia, "Graphene metalens for particle nanotracking," Photon. Res. **8**, 1316–1322 (2020).
28. F. Ding, Y. T. Chen, and S. I. Bozhevolnyi, "Gap-surface plasmon metasurfaces for linear-polarization conversion, focusing, and beam splitting," Photon. Res. **8**, 707–714 (2020).
29. W. G. Liu, B. Hu, Z. D. Huang, H. Y. Guan, H. T. Li, X. K. Wang, Y. Zhang, H. X. Yin, X. L. Xiong, J. Liu, and Y. T. Wang, "Graphene-enabled electrically controlled terahertz meta-lens," Photon. Res. **6**, 703–708 (2018).
30. H. X. Xu, S. J. Ma, W. J. Luo, T. Cai, S. L. Sun, Q. He, and L. Zhou, "Aberration-free and functionality-switchable meta-lenses based on tunable metasurfaces," Appl. Phys. Lett. **109**, 193506 (2016).
31. Z. Zhang, D. Wen, C. Zhang, M. Chen, W. Wang, S. Chen, and X. Chen, "Multifunctional light sword metasurface lens," ACS Photon. **5**, 1794–1799 (2018).
32. X. Zang, W. Xu, M. Gu, B. Yao, L. Chen, Y. Peng, J. Xie, A. V. Balakin, A. P. Shkurinov, Y. Zhu, and S. Zhuang, "Polarization-insensitive metalens with extended focal depth and longitudinal high-tolerance imaging," Adv. Opt. Mater. **8**, 1901342 (2019).
33. Y. Fan, B. Cluzel, M. Petit, X. Le Roux, A. Lupu, and A. de Lustrac, "2D waveguided Bessel beam generated using integrated metasurface-based plasmonic axicon," ACS Appl. Mater. Interfaces **12**, 21114–21119 (2020).
34. Y. Li, B. Liang, Z. M. Gu, X. Y. Zou, and J. C. Cheng, "Reflected wavefront manipulation based on ultrathin planar acoustic metasurfaces," Sci. Rep. **3**, 2546 (2013).
35. S. Liu, A. Noor, L. L. Du, L. Zhang, Q. Xu, K. Luan, T. Q. Wang, Z. Tian, W. X. Tang, J. G. Han, W. L. Zhang, X. Y. Zhou, Q. Cheng, and T. J. Cui, "Anomalous refraction and nondiffractive Bessel-beam generation of terahertz waves through transmission-type coding metasurfaces," ACS Photon. **3**, 1968–1977 (2016).
36. X. Li, M. Pu, Z. Zhao, X. Ma, J. Jin, Y. Wang, P. Gao, and X. Luo, "Catenary nanostructures as compact Bessel beam generators," Sci. Rep. **6**, 20524 (2016).
37. H. Gao, M. Pu, X. Li, X. Ma, Z. Zhao, Y. Guo, and X. Luo, "Super-resolution imaging with a Bessel lens realized by a geometric metasurface," Opt. Express **25**, 13933–13943 (2017).
38. E. Arbabi, A. Arbabi, S. M. Kamali, Y. Horie, and A. Faraon, "Multiwavelength polarization-insensitive lenses based on dielectric metasurfaces with meta-molecules," Optica **3**, 628–633 (2016).
39. W. T. Chen, A. Y. Zhu, J. Sisler, Z. Bharwani, and F. Capasso, "A broadband achromatic polarization-insensitive metalens consisting of anisotropic nanostructures," Nat. Commun. **10**, 355 (2019).
40. M. Khorasaninejad, A. Y. Zhuit, C. Roques-Carmes, W. T. Chen, J. Oh, I. Mishra, R. C. Devlin, and F. Capasso, "Polarization-insensitive metalenses at visible wavelengths," Nano Lett. **16**, 7229–7234 (2016).
41. X. Li, L. Chen, Y. Li, X. Zhang, M. Pu, Z. Zhao, X. Ma, Y. Wang, M. Hong, and X. Luo, "Multicolor 3D meta-holography by broadband plasmonic modulation," Sci. Adv. **2**, e1601102 (2016).
42. X. Zhang, X. Li, J. Jin, M. Pu, X. Ma, J. Luo, Y. Guo, C. Wang, and X. Luo, "Polarization-independent broadband meta-holograms via polarization-dependent nanoholes," Nanoscale **10**, 9304–9310 (2018).
43. K. Huang, Z. Dong, S. Mei, L. Zhang, Y. Liu, H. Liu, H. Zhu, J. Teng, B. Luk'yanchuk, J. K. W. Yang, and C. W. Qiu, "Silicon multi-meta-holograms for the broadband visible light," Laser Photon. Rev. **10**, 500–509 (2016).
44. K. E. Chong, L. Wang, I. Staude, A. R. James, J. Dominguez, S. Liu, G. S. Subramania, M. Decker, D. N. Neshev, I. Brener, and Y. S. Kiyshar, "Efficient polarization-insensitive complex wavefront control using Huygens' metasurfaces based on dielectric resonant meta-atoms," ACS Photon. **3**, 514–519 (2016).
45. L. Wang, S. Kruk, H. Tang, T. Li, I. Kravchenko, D. N. Neshev, and Y. S. Kivshar, "Grayscale transparent metasurface holograms," Optica **3**, 1504–1505 (2016).
46. H. X. Xu, T. Cai, Y. Q. Zhuang, Q. Peng, G. M. Wang, and J. G. Liang, "Dual-mode transmissive metasurface and its applications in multi-beam transmitarray," IEEE Trans. Antennas Propag. **65**, 1797–1806 (2017).
47. A. H. Abdelrahman, A. Z. Elsherbeni, and F. Yang, "Transmission phase limit of multilayer frequency-selective surfaces for transmitarray designs," IEEE Trans. Antennas Propag. **62**, 690–697 (2014).
48. T. Shi, Y. J. Wang, Z. L. Deng, X. Ye, Z. X. Dai, Y. Y. Cao, B. O. Guan, S. M. Xiao, and X. P. Li, "All-dielectric kissing-dimer metagratings for asymmetric high diffraction," Adv. Opt. Mater. **7**, 1901389 (2019).
49. A. B. Evlyukhin, C. Reinhardt, and B. N. Chichkov, "Multipole light scattering by nonspherical nanoparticles in the discrete dipole approximation," Phys. Rev. B **84**, 235429 (2011).
50. P. Grahn, A. Shevchenko, and M. Kaivola, "Electromagnetic multipole theory for optical nanomaterials," New J. Phys. **14**, 093033 (2012).